Effect of Wing Flexibility on Lift and Thrust Production in Flapping Flight

Pradeep Gopalakrishnan* and Danesh K. Tafti†

Virginia Polytechnic Institute and State University, Blacksburg, Virginia 24061

In bird and insect flight, wing deformation plays an important role in aerodynamic performance. The wing deformation is produced by neuromuscular control and/or by aeroelastic effects. The focus of the current study is to evaluate the effects of wing deformation by coupling a large-eddy simulation solver with a linear elastic membrane model. Different membrane prestresses are investigated to give a desired camber in response to the aerodynamic pressure. All simulations are carried out at $Re = 10,000$ for forward flight with an advance ratio of 0.5. The results show that the camber introduced by a flexible wing increases the thrust and lift production considerably. An analysis of flow structure reveals that, for flexible wings, the leading-edge vortex stays attached on the top surface of the wing and glides along the camber and covers a major part of the wing, which results in high force production. On the other hand, for rigid wings, the leading-edge vortex lifts off from the surface resulting in lower force production. Further, introduction of the camber also increases the force component contributing to thrust, leading to a high thrust-to-lift ratio. In comparison to a rigid wing, a 40% increase in thrust is observed for the low-prestress case, which results in a camber of 0.25 chord. Further, the results also show that the wing with high spanwise prestress and low chordwise prestress offers better performance both in terms of force production and uniformity in the force-induced cambering.

Nomenclature

C	=	airfoil chord length
C_L	=	coefficient of lift
C_T	=	coefficient of thrust
$F_{x/y}$	=	force acting on the wing
f	=	frequency of flapping
h	=	wing thickness
J	=	advance ratio, U_∞/U_f; ratio of the flight velocity to the flapping velocity
N_ξ	=	prestress along the chord
$N_{\xi\zeta}$	=	prestress in shear
N_ζ	=	prestress along the span
P	=	power required
p	=	pressure
R	=	semiwingspan; distance from flapping axis to wing tip
Re	=	Reynolds number, $U_f C/\nu$
Re_t	=	inverse of the turbulent viscosity
r	=	distance from flapping axis
U_f	=	flapping velocity at tip, $2\Phi f R$
U_∞	=	freestream velocity; forward flight velocity
u_f	=	local flapping velocity
w	=	out-of-plane deformation
$\mathbf{x}$	=	fixed reference coordinate
α	=	angle of attack
β	=	stroke plane angle
η_{prop}	=	propulsive efficiency
ν	=	kinematic viscosity
$\boldsymbol{\xi}$	=	moving reference coordinate
ρ	=	torsional angle
ρ_a	=	density of air
ρ_w	=	density of wing
τ	=	shear stress on the surface of the wing
Φ	=	total flapping amplitude (maximum to minimum)
ϕ	=	flapping angle
Ω	=	angular velocity of the wing
ω	=	vorticity

Subscripts

d	=	downstroke
eff	=	effective
u	=	upstroke
x, y, z	=	fixed reference coordinates
ξ, η, ζ	=	moving reference coordinates

*Graduate Student, Mechanical Engineering, 114K, Randolph Hall. Student Member AIAA.

†Professor, Mechanical Engineering, 114I, Randolph Hall. Member AIAA.

I. Introduction

FLAPPING flight is highly suitable for micro air vehicles (MAVs), which by requirement are compact with dimensions of less than 15–20 cm, have flight speeds of around 10–15 m/s and gross takeoff weights of 200 g or less, and operate in the low-Reynolds-number (10^4–10^5) regime. At these low Reynolds numbers, the aerodynamic efficiency (lift-to-drag ratio) of conventional fixed airfoils deteriorates rapidly [1]. On the other hand, birds and insects whose flight regime coincides with that of MAVs use flapping flexible wings to overcome the disadvantages of steady aerodynamics. The kinematics involved in normal canonical flapping flight is divided into two translation motions corresponding to the up and down strokes and two rotational motions (pronation before the downstroke and supination before the upstroke) corresponding to stroke reversals.

A number of unsteady aerodynamic mechanisms such as clap and fling [2], delayed stall [3,4], wake capturing [5], and rotational circulation [5] have been proposed to explain the generation of lift in birds and insects. Among these, the delayed stall mechanism, which involves the formation of a stable leading-edge vortex (LEV), is the primary mechanism used by most birds and insects for production of lift during wing translation. During the downstroke, air swirls around the leading edge and forms a LEV. This LEV increases the bound vortex circulation and, hence, the lift. In a fixed airfoil, the formation of the LEV leads to dynamic stall within 3–4 chord lengths of travel. However, in insects, the LEV remains stable for the entire downstroke, during which it covers a distance of more than 8 chord lengths.

The stability of the LEV plays an important role in the superior performance of birds and insects. Many previous studies [5–8] evaluated the duration and stability criteria of the LEV. Ellington [6] conducted flow visualization studies using a large mechanical model of a hawk moth, *flapper* ($Re \sim 4000$). An intense LEV on the downstroke at all flight speeds (0.4–5.7 m/s) was observed. The LEV spiraled out toward the wing tip with a high spanwise velocity comparable to the flapping velocity, which stabilized the vortex. The LEV structure was similar to the conical leading-edge vortex found in delta wings. They suggested that the strong spanwise flow was created by the pressure gradient formed due to the velocity gradient along the flapping wing, by the centrifugal acceleration in the boundary layer, or by the induced velocity field of the spiral vortex lines.

In our previous study [9,10], we analyzed the flow structure of the LEV for forward flight at an advance ratio of 0.5 with various rotation kinematics and angles of attack. The results showed the formation of a spiral LEV with strong spanwise flow along its core for all kinematic conditions. However, a negative spanwise flow near the tip induced by the presence of a tip vortex led to the instability of the LEV and its separation from the wing during the middle of the downstroke. Despite the instability, the LEV contributes significantly to thrust and lift, and proves to be the dominant mechanism in flapping flight.

In addition to the basic kinematics, birds and insects employ large-scale deformation of their wing geometries to improve the aerodynamic efficiency through neuromuscular control and/or through the aeroelastic response of the wings. Wang et al. [11] measured the kinematics of dragonfly flight for forward and maneuvering flight conditions. Their results showed that the camber varied significantly from −0.1 to 0.12 due to wing flexibility during the flapping cycle. They also conducted flow analysis of a 2-D model of a dragonfly with and without camber variation and showed that camber significantly affected the lift production. The study on a hovering hummingbird by Tobalske et al. [12] showed the importance of camber on lift generation. Despite the kinematic symmetry of the upstroke and downstroke, the humming bird generated 75% of the lift during the downstroke due to positive camber and generated only 25% during the upstroke due to the absence of a negative camber. Liu et al. [13] measured the wing geometry and kinematics of a seagull, merganser, teal, and owl and observed that the wing sections are highly cambered ($0.085C$) and are similar to the low-Reynolds-number airfoil S1223.

The wing deformation of birds and insects significantly affects the stability and strength of the LEV and force production. For the numerical analysis of deforming wings, a solver capable of solving both the fluid and structural equations is necessary. Here, a brief review of previous studies focused on aeroelastic analysis related to MAVs for both fixed and flapping wings is provided. Shyy et al. [14] and Ho et al. [15] provided a detailed review of the performance of flexible fixed wings for MAVs. Shyy et al. [16] analyzed the performance of a stationary airfoil at a Reynolds number of 7.5×10^4 in a sinusoidal freestream with three different types of flexibility; rigid, flexible, and hybrid. The initial camber of all airfoils was fixed to get an incident angle of 6 deg. In the case of the flexible airfoil, the camber was allowed to change above and below the initial camber, whereas in the case of the hybrid airfoil, a decrease in camber was prevented by a wire construction beneath the flexible membrane. The results showed that the flexible airfoil had a higher sensitivity to freestream fluctuation and produced a higher lift-to-drag ratio than the fixed airfoil at high velocities. However, the camber of the flexible membrane collapsed at low velocity due to freestream fluctuations, which resulted in massive separation over the whole surface. On the other hand, the hybrid airfoil with a lower limit on the camber was less sensitive to freestream fluctuation and produced superior performance at all flow velocities. Shyy et al. [17] analyzed the effect of a flexible membrane placed on top of the Clary-Y airfoil on the aerodynamic performance. The flexible membrane adjusted the profile based on the fluctuation of the freestream, which resulted in better performance.

Smith [18] included aeroelastic effects while analyzing the flapping flight of a tethered moth using an unsteady panel method. He modeled the veins in the wing as three-dimensional tubular beam elements and the wing surface as a quadrilateral orthotropic plane stress membrane. The unsteady panel method employed did not account for the separation at the leading edge, which resulted in a deviation of the computed force from the experimental results. Ho et al. [15] compared the aerodynamic performance of a cicada wing, which is rigid along the spanwise direction, with a flexible titanium alloy wing without leading-edge support. The results showed that the stiffness along the leading edge was critical for the stability of the LEV, as the cicada wing produced higher lift than the flexible wing. They also showed that stiffness distribution is a key parameter in defining vortex interaction and thrust production. Their results showed that high stiffness is required at the outboard region of the wing to enhance lift, with wing flexibility required at the inward region for producing thrust.

Stanford and Ifju [19] and Stanford et al. [20] analyzed the effect of a flexible membrane on a fixed airfoil with both experiments and numerical modeling. They modeled the membrane as inextensible using a linear stress-stiffening model. The linear stress-strain assumption held well, because the strain accumulated due to the aerodynamic load was small in comparison with the prestrain of the membrane. Their results showed that the efficiency of the rigid wing increased with Reynolds number, because the flexible membrane provided a nonoptimal airfoil shape at high Reynolds numbers. Stanford et al. [21] analyzed flow over a flexible fixed wing using a static aeroelastic model by coupling a laminar flow solver and a structural membrane solver. They compared the numerical results with experiments and showed that the numerical model failed to predict the exact location of separation and reattachment. They identified that the unsteady nature of the flow, turbulence effects, and membrane wrinkling are the primary reasons for the poor performance of the static aeroelastic model.

Previous research on flapping flight has focused mainly on the aerodynamics of rigid wings. However, kinematic studies show that birds and insects undergo significant wing deformation to improve aerodynamic efficiency. Further, aeroelastic studies on fixed wings show that flexible wings offer better performance than rigid wings. Because of unsteadiness, flow separation, and turbulence, previous studies using panel methods and simplified laminar solvers have failed to capture the exact effect of membrane wings on performance. The present study addresses this issue by analyzing flapping flight for a flexible wing at $Re = 10,000$ using an unsteady large-eddy simulation (LES) flow solver coupled with a linear elastic membrane wing model. The focus of the study is to evaluate the effect of aerodynamic-induced camber on the strength and stability of the LEV. The wing is treated as an elastic membrane with in-plane prestresses. The prestresses of the wing are tailored to induce a camber in the range of 0.1–0.25 times the chord length, and their effect is analyzed based on changes in flow structure and on variation of thrust and lift.

II. Methodology

The unsteady aerodynamics of the flapping wing is solved using LES on a deforming body-fitted fluid mesh using a multiblock finite volume methodology. Details about the flow solver are presented in many of our previous studies [9,10,22,23].

A. Elastic Membrane Model

This section presents details about the membrane model employed for the flexible wing. In the present study, the wing is modeled as a linear elastic membrane structure which is prestressed by stretching at its boundaries. The out-of-plane deformation is computed using the nondimensional dynamic membrane equation [24] in the wing reference coordinate:

$$N_\xi \frac{\partial^2 w}{\partial \xi^2} + 2N_{\xi\zeta} \frac{\partial^2 w}{\partial \xi \partial \zeta} + N_\zeta \frac{\partial^2 w}{\partial \zeta^2} + p = \rho_w h_w \frac{\partial^2 w}{\partial t^2} \qquad (1)$$

where w is the out-of-plane displacement, p is the applied aerodynamic differential pressure across the wing, ρ_w is density of the wing, h_w is the wing thickness, and N_ξ, N_ζ, and $N_{\xi\zeta}$ are the chordwise,

Table 1 Membrane tensile force-per unit length non-dimensional values and dimensional value corresponding to $C = 2$ cm

Simulation	N_ξ		N_ζ	
	Nondimensional	N/m	Nondimensional	N/m
Rigid	——	——	——	——
Case A	5.208	8	5.208	8
Case B	2.604	4	2.604	4
Case C	1.302	2	1.302	2
Case D	1.302	2	5.208	8
Case E	5.208	8	1.302	2

**Table 2 Kinematic parameters and nondimensional numbers for flapping flight**

Parameters	Description
Stroke plane	The plane defined by three points: wing base (B), wing tip at maximum (T_T), and minimum angular position (T_B). During hovering the stroke plane will be near horizontal, and during forward flight it will be vertical.
Stroke plane angle, β	Angle between the stroke plane and the horizontal plane. It ranges from 0 deg for hovering to 90 deg for forward flight.
Angle of attack, α	Angle between the wing direction (from trailing edge to leading edge) and the direction of motion.
Torsional angle, ρ	Angle between the wing direction and the direction perpendicular to the stroke plane.
Flapping angle, ϕ	Angle between the leading edge of the wing and the horizontal plane.
Reynolds number, $U_f C/\nu$	Defined based on midspan chord length, c, and flapping velocity, $U_f = 2\Phi f R$, where Φ is the total flapping amplitude (max to min), R is the half-span (axis to wing tip), and f is the frequency of flapping
Advance ratio, $J = U_\infty/U_f$	Ratio of the flight velocity to the flapping velocity

spanwise, and in-plane shear prestresses per unit membrane length, respectively. The equation is nondimensionalized with the same characteristic parameters used for the flow solver, chord length (C), and flapping velocity (U_f). The prestresses are normalized by $\rho_a U_f^2 C$, and $\rho_w h_w$ is normalized by $\rho_a C$. A zero displacement boundary condition is specified at all edges of the wing. In practice, the linear assumption employed in Eq. (1) is strictly valid only if the strain accumulated by the deformation is small in comparison to the prestrain in the membrane. However, for simplification, the present study employs a linear assumption for all the prestress values studied. Further, the inertial forces due to flapping are not considered in the current study. The implications of these assumptions on the results are discussed later.

B. Coupling

An explicit time advancement method using the latest available information is employed for coupling between the flow solver and the membrane solver. The steps involved in coupling are as follows:

1) The flow is advanced to time level $n + 1$ with known deformation values at n.

2) The pressure values are transferred from the fluid solver to the membrane solver. Because the same grid distribution is used for both solvers, no interpolations are necessary.

3) The membrane solver is advanced using the pressure values at time level $n + 1$ with known deformation at level n and $n - 1$. A second-order central difference at time level n is employed for both spatial and temporal derivatives.

4) The deformation values are then transferred to the flow solver.

5) Steps 1–4 are repeated for the next time advancement.

III. Results

The main focus of the study is to evaluate the effects of aeroelastic cambering on flow structures and aerodynamic performance. To estimate their effects, simulations with different prestresses (cases A–C) as given in Table 1 are carried out and the resulting performance is compared against that of a rigid wing. The prestress

values (N_ξ and N_ζ) are tailored to obtain the camber in the order of 0.05–0.25 chord, and the prestress in shear $N_{\xi\zeta}$ is kept at zero for all the simulations. In addition, different prestresses are used in the spanwise and chordwise directions to analyze their effects on performance (cases D and E). All the simulations are carried out at $Re = 10,000$ and an advance ratio of $J = 0.5$. For a chord length of $C = 2$ cm, this corresponds to a flapping velocity of $U_f = 8$ m/s ($f = 47.75$ Hz) and a forward velocity of $U_\infty = 4$ m/s at standard conditions. For a chord length of $C = 4$ cm, this corresponds to $U_f = 4$ m/s ($f = 11.94$ Hz) and a forward velocity of $U_\infty = 2$ m/s. For aeroelastic analysis, the material properties of polyester $\rho_w = 1350$ kg/m^3 with thickness of h_w of 0.05 mm are used.

A. Wing Configuration and Kinematics

Figure 1 shows the important kinematic parameters of flapping flight, with their definitions given in Table 2.

In the present study, a rectangular wing with an aspect ratio of 4 from base to tip as shown in Fig. 2a is used for the analysis of flapping flight. The pitching axis is placed at one-fourth of a chord length from the leading edge. The coordinates x, y, and z are used for the fixed frame, where the y–z plane represents the stroke plane (Fig. 1) for a stroke plane angle of $\beta = 90$ deg. The coordinates ξ, η, and ζ are used for the moving frame fixed with the wing, where ξ is along the chordwise direction, η is perpendicular to the wing, and ζ is along the
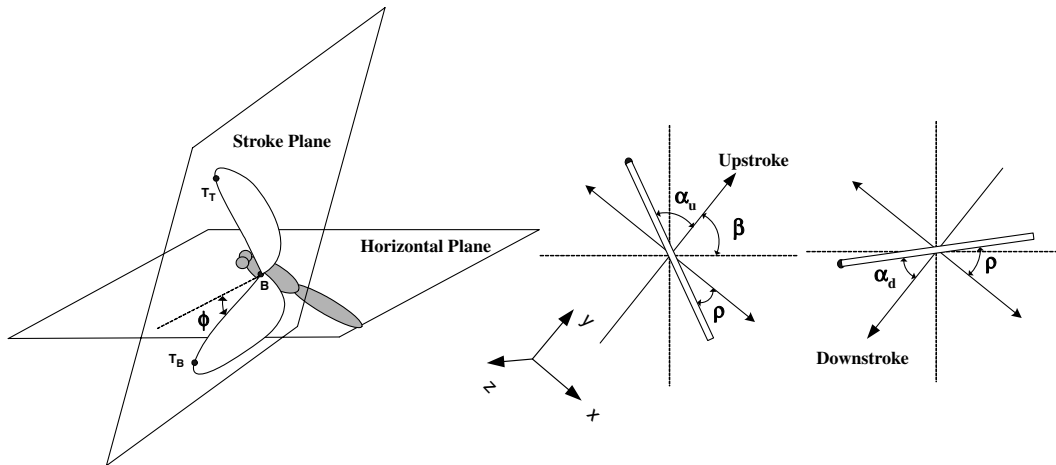
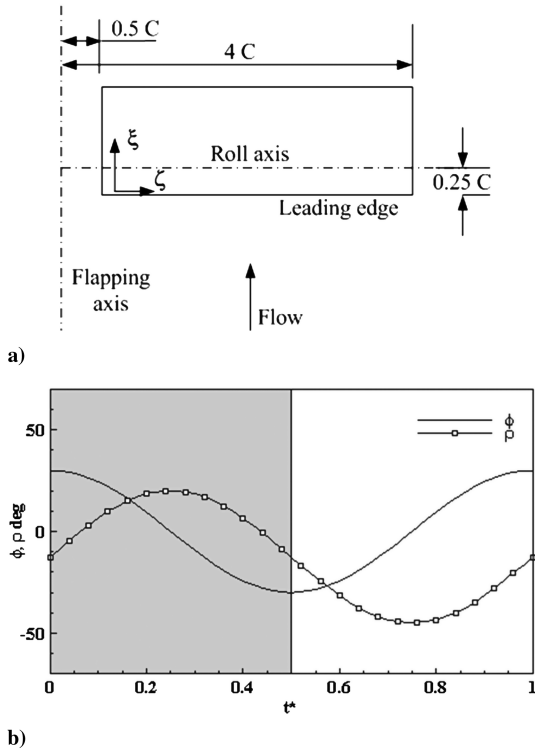**Fig. 1 Kinematic parameters.**

a)

b)

Fig. 2   Wing configuration and kinematics: a) dimensions of the wing, and b) variation of flapping and torsional angle. The shaded region represents downstroke.
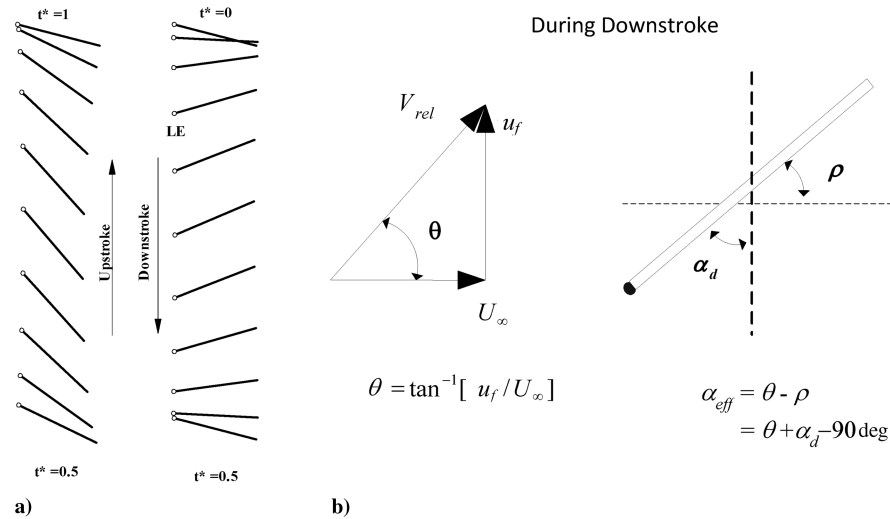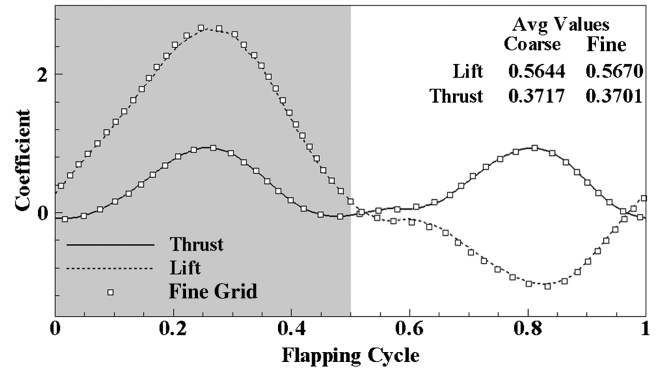

Fig. 5   Comparison of lift and drag for different grid sizes.

spanwise direction (Fig. 2a). A sinusoidal variation of flapping angle and torsional angle with a flapping amplitude of $\Phi = 30$ deg as shown in Fig. 2b is used for the kinematics. The t^* value ranges from 0 to 0.5 for the downstroke and 0.5 to 1 for the upstroke. The selection of kinematics is based on the results from our previous analysis on the effect of rotation kinematics [9,10], which showed that continuous rotation resulted in high thrust. The movement of the wing tip for the prescribed kinematics is shown in Fig. 3a. During the start of the translation, the angle of attack, α, is close to 90 deg, and it drops during the first half to its lowest value and increases to the initial value during the second half of the translation. The α_d during the middle of the downstroke is 75 deg and during the upstroke α_u is 45 deg. A lower value of angle of attack during the upstroke is used to reduce the downward force. The effective angle of attack depends on the
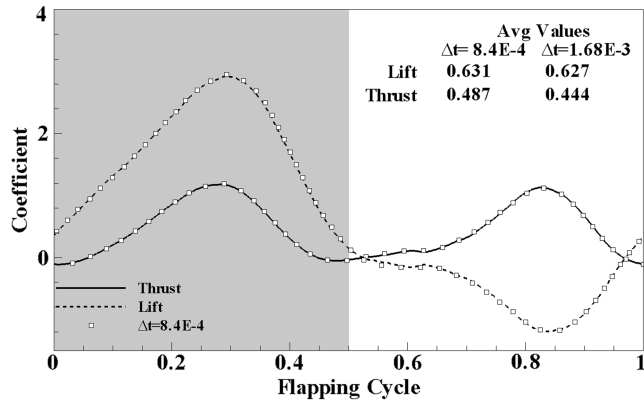

a)   b)

Fig. 3   Variation of angle of attack: a) wing positions at different times, and b) effective angle of attack during the downstroke.

a)   b)   c)
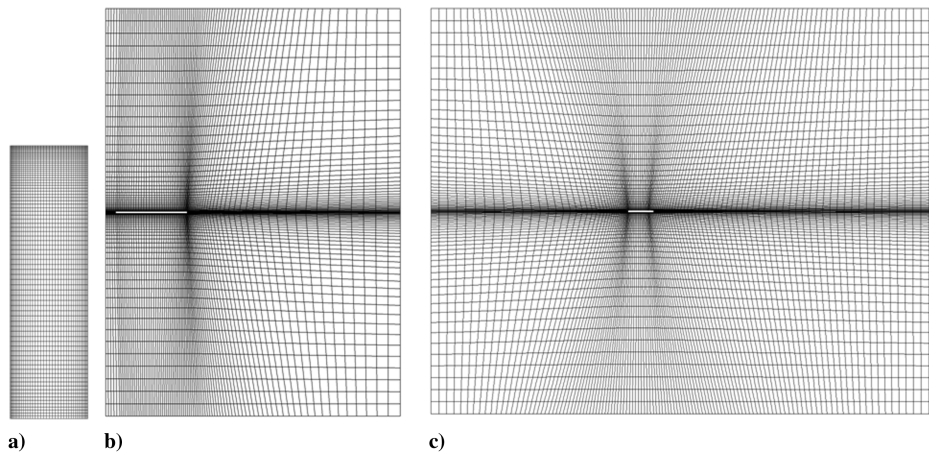
Fig. 4   Grid distribution: a) wing, b) spanwise plane, and c) chordwise plane. Every other grid line is shown for Figs. 4b and 4c.

Fig. 6 Comparison of lift and thrust coefficient profiles at $\Delta t = 1.68 \times 10^{-3}$ and 8.4×10^{-4}.

local flapping velocity, freestream velocity, and prescribed angle of attack (α_u, α_d) as shown in Fig. 3b. Because of the variation of wing flapping velocity along the spanwise direction, the effective angle of attack also varies along the span with a maximum value at the tip.

B. Computational Grid and Validation

The validation of the dynamic moving grid solver was carried out with a heaving airfoil and forced oscillations of a cylinder in crossflow, which are available in our previous studies [22,23]. Further, an analysis of a hovering fruit fly was also carried out [10] and the resultant aerodynamic forces compared well with experimental results.

In this study, the aerodynamic grid is made of 60 blocks with approximately 6.5×10^6 cells. The flow domain is defined from 10 chord lengths upstream of the leading edge and extends 15 chord lengths downstream from the trailing edge. In the direction normal to

the wing, the flow domain extends 10 chord lengths on either side. The domain also extends 10 chord lengths in the spanwise direction from the tip. A constant velocity boundary condition is applied at all inlet faces and an outflow boundary condition is specified at the downstream boundary. The symmetry condition is applied along the flapping axis at the base of the wing. The wing is resolved using 80×40 grid points, and 80 grid points are used perpendicular to the wing as shown in Fig. 4. A grid refinement study is carried out by increasing the number perpendicular to the wing from 80 to 120. The instantaneous lift and thrust forces for fine and coarse grids are shown in Fig. 5. The profiles compare well and the cycle-averaged values of lift and thrust differ by less than 1%.

The structural solver is verified separately by the method of manufactured solutions. A known profile is assumed for the displacement, w, and the pressure source term, p, corresponding to that profile is computed analytically from Eq. (1). The membrane solver was tested with the analytical source term and the resultant displacement was compared against the analytical profile w to verify the solution accuracy. In addition, to check the accuracy of the coupling between the flow and membrane solver, a time-step independency study is carried out for case B by reducing the time step by a factor of 2 from the nominal nondimensional time step of $\Delta t = 1.68 \times 10^{-3}$ to $\Delta t = 8.4 \times 10^{-4}$. A comparison of the instantaneous lift and thrust profiles in Fig. 6 show very small differences between the two time steps; less than 1% difference is obtained in the mean coefficient values, implying that the sequential explicit coupling between the fluid and membrane solvers resolved at $\Delta t = 1.68 \times 10^{-3}$ adequately captures the coupled dynamics.

C. Rigid Wing Performance

Before analyzing the effect of the flexible membrane on performance, critical flow structures obtained for a rigid wing are presented in this section. The results obtained during the fourth flapping cycle are used for the analysis.
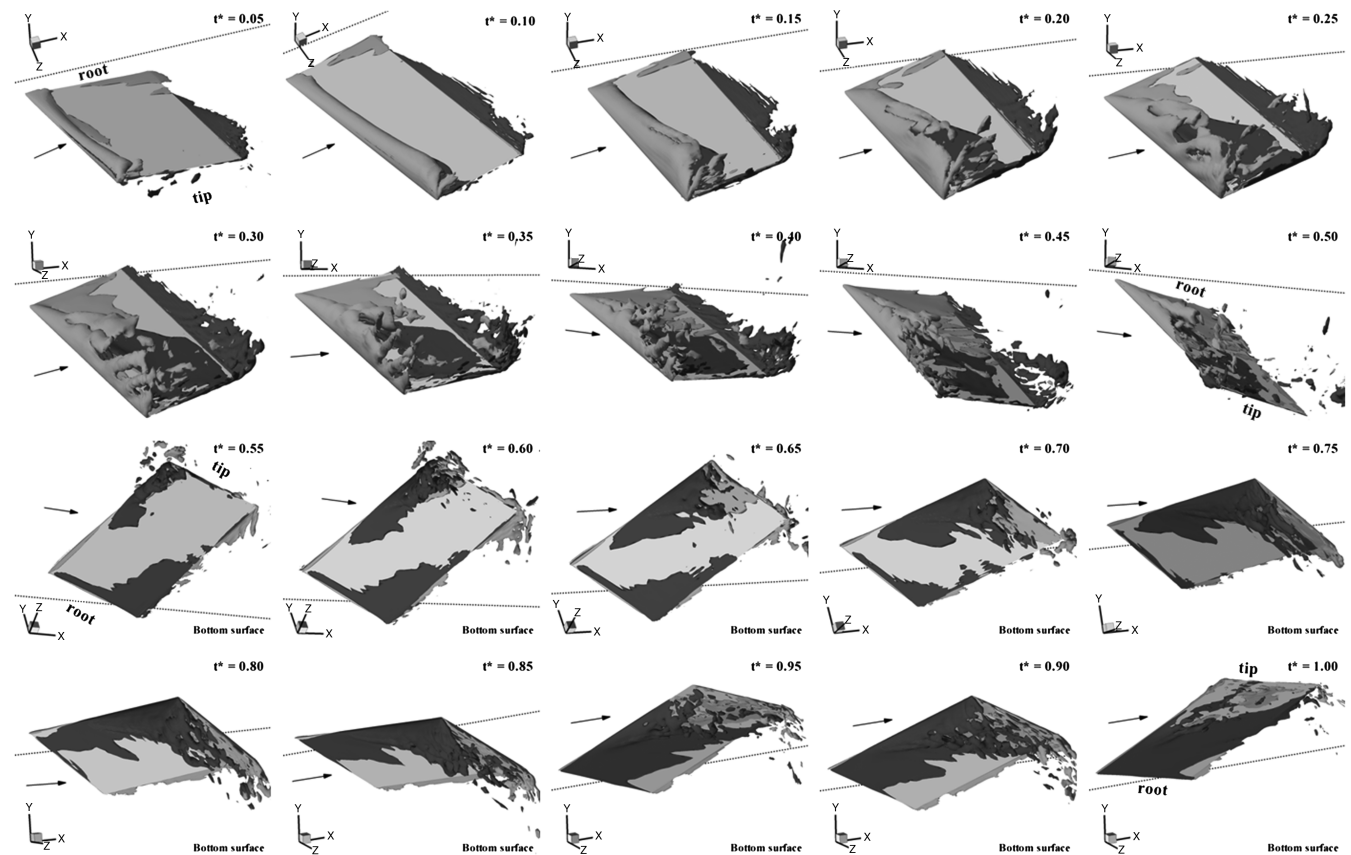

Fig. 7 Isosurface of spanwise vorticity ω_ζ at different times for the rigid wing. The arrows near the leading edge represent the flow direction, and the dotted lines represent the flapping axis; root and tip of the wing are marked for better visualization; during upstroke ($t^* = 0.55$–1.00), the figure shows the bottom surface of the wing.
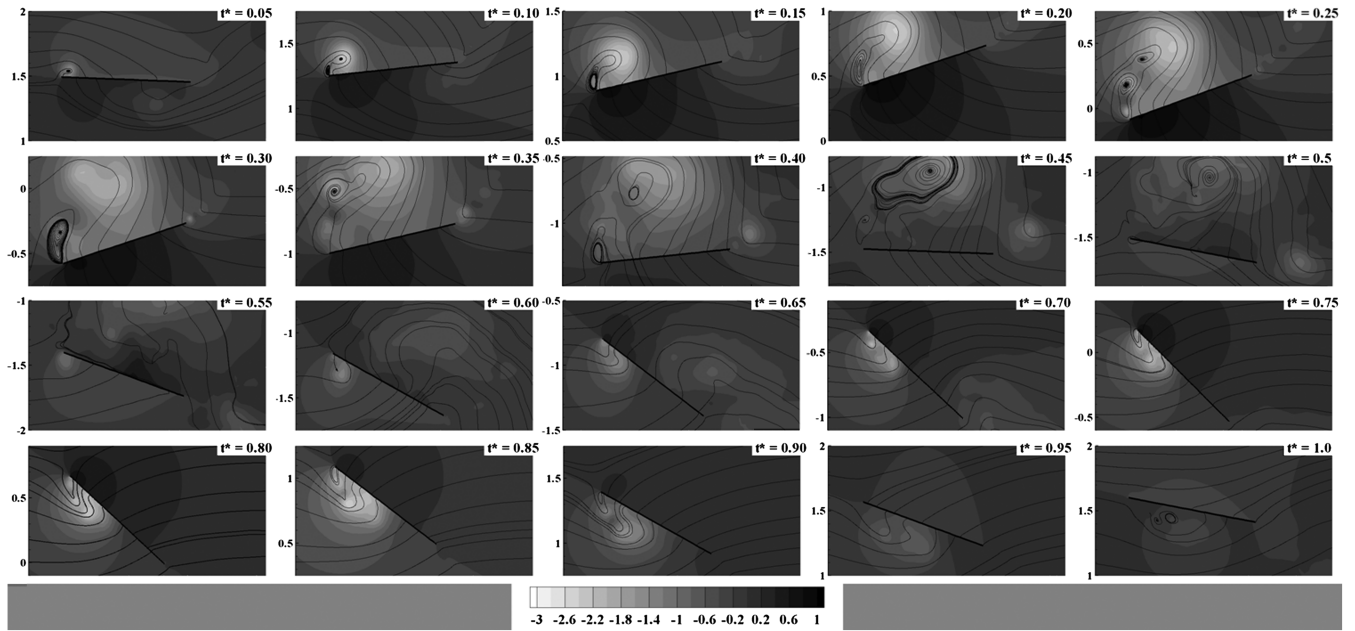
Fig. 8   Instantaneous pressure contours and streamlines in a chordwise plane at $\zeta = 3$ for the rigid wing.

1. During Downstroke

The isosurface of vorticity along the spanwise direction in wing reference frame ω_ζ at different times is given in Fig. 7. The isosurfaces show the formation of a LEV (negative vorticity) and its subsequent separation during the downstroke. At $t^* = 0.05$, a spiral LEV with size gradually increasing from base to tip forms on the top surface of the wing. The size of the LEV grows with time until its separation. At $t^* = 0.2$, the spiral LEV is the strongest, resulting in a peak in lift (Fig. 5). The pressure contours and streamlines in the chordwise plane, $\zeta = 3$, in Fig. 8 show detailed slices of the LEV evolution and separation. The LEV starts to lift away from the wing as early as $t^* = 0.1$, and its separation leads to the formation of multiple secondary LEVs. The secondary LEVs also lift away from the surface of the wing and the pressure contours show the detachment of the LEV (low-pressure region) and an increase in pressure on the surface of the wing by the entrainment of freestream fluid. The isosurface of the vorticity shows that the LEV near the root is attached for most of the downstroke, whereas the LEV near the tip sheds and completely dissipates into the flow during the end of the downstroke ($t^* = 0.4$–0.5). The vorticity contours also show the growth of a trailing-edge vortex (TEV) during the downstroke, with its maximum size near the tip. The TEVs are also shed at the end of the downstroke ($t^* = 0.4$–0.5) and dissipate into the flow.

To analyze the LEV structure, particle traces are obtained by releasing particles along the leading edge. The particle traces at $t^* = 0.25$ in Fig. 9a show a spiral LEV attached near the base and lifted from the wing near the tip. The spanwise velocity v_ζ contours along the center of the LEV in Fig. 9b show a strong positive

velocity of the order of the flapping velocity from the base to the tip. Similar results were obtained by the flow visualization studies conducted by Ellington [6] using a large mechanical model of a hawk moth at $Re \sim 4000$. Ellington showed a spiral LEV with a spanwise velocity comparable to the flapping velocity during the downstroke and suggested that the spanwise flow removed the vorticity from the LEV and stabilized it. However, the present results show that, despite the presence of the spanwise flow, the LEV separates from the wing as early as $t^* = 0.1$. We surmise that the presence of strong negative spanwise velocity due to the tip vortex shown by the curved arrow in Fig. 9b is the primary reason for the separation of the LEV, as it prevents the removal of vorticity from the LEV. The vorticity starts building up near the tip, due to both the high angle of attack and the convection of vorticity from the base. This increase in vorticity leads to an instability in the LEV and its separation from the wing near the tip.

2. During Upstroke

The behavior of flow during the upstroke is similar to that during the downstroke. During the upstroke, the angle of attack is relatively low and the effective angle of attack is negative only for a small portion of the wing near the tip. Hence, there is no clear formation of the LEV on the bottom surface, and the vorticity contours in Fig. 7 show only a small positive vortex attached near the tip. The streamlines and pressure contours in Fig. 8 show no apparent vortex formation at $\zeta = 3.0$. A small low-pressure region and multiple small LEVs are observed at around $t^* = 0.8$. This low-pressure region
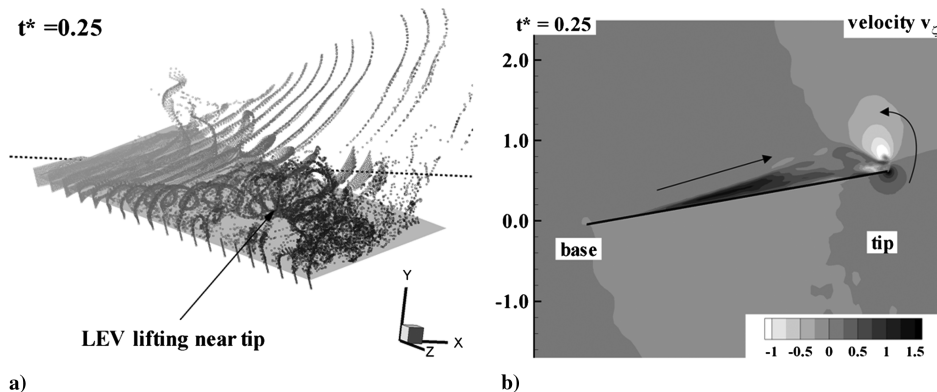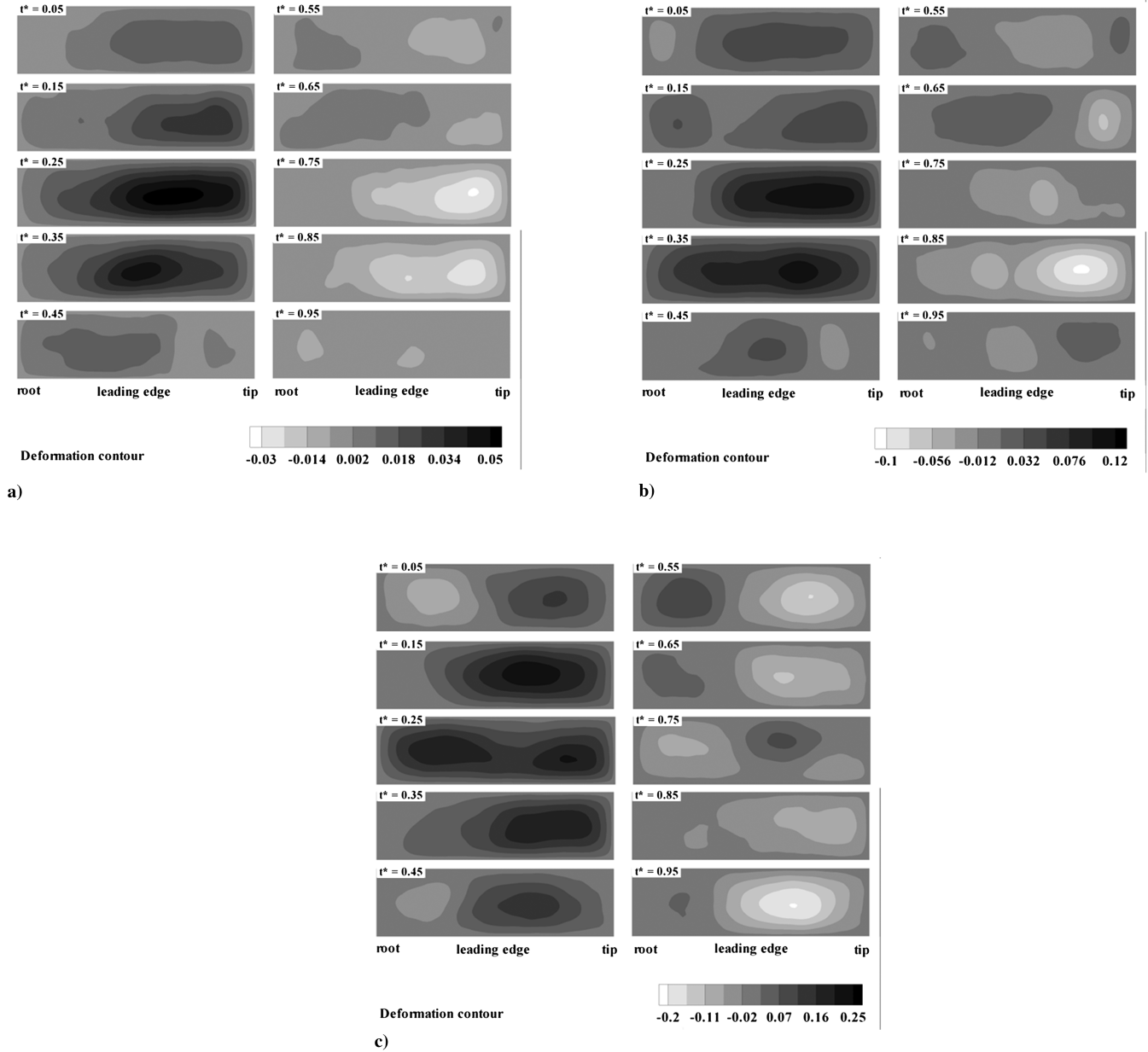

Fig. 9   LEV structure at $t^* = 0.25$: a) particle trace, and b) spanwise velocity along the center of the LEV.

Fig. 10   Deformation contours during the flapping cycle for prestress: a) 8 N/m b) 4 N/m, and c) 2 N/m.

results in a peak in negative lift and also generates thrust (Fig. 5). These LEVs become unstable and shed at the end of the upstroke.

D.   Effect of Flexible Wing

To analyze the effects of aeroelastic deformation on the flow structure, three simulations (cases A–C) with different prestresses are carried out. The deflection for the cases ranges from 0.05 to 0.25 chord. For maximum thrust production, positive deflection during the downstroke and negative deflection during the upstroke are preferred. Figure 10 shows the deformation contour (different scales are used) at different times for all three cases. During the downstroke, the deformation is positive, which introduces a positive camber. The maximum value of deformation near the tip corresponds to the location where the size of the LEV and the pressure difference across the surface are maximum. For cases A ($N_\xi = N_\zeta = 8$ N/m) and B ($N_\xi = N_\zeta = 4$ N/m), the camber reaches a maximum during the middle of the downstroke (at $t^* = 0.25$) and the deformation introduces a smooth camber with one peak displacement close to the tip of the wing. For case C ($N_\xi = N_\zeta = 2$ N/m), the deformation at the start of the downstroke is negative near the base and positive near the tip. The negative displacement near the base is due to the presence

of a low-pressure region on the bottom surface created during the previous upstroke. In addition, the deformation during the middle of the downstroke introduces an uneven camber with two peaks, one near the base and one near the tip.

During the upstroke, a negative camber forms for all the simulations and its maximum value is lower than that during the downstroke due to a low angle of attack. The time of formation of the negative camber differs significantly between the three cases. For the high-prestress case, case A, the maximum camber occurs at around $t^* = 0.75$, whereas the maximum camber occurs at $t^* = 0.85$ and 0.95 for cases B and C, respectively. For the low-prestress membrane, case C, at the start of the upstroke the deformation is positive near the base due to the presence of an unshed LEV from the previous downstroke.

1.   Effect on Flow Structure

The effect of camber on flow structure is shown by the vorticity contours at different times for all three cases in Fig. 11, and the streamlines and pressure contours in the chordwise plane at $\zeta = 3$ are shown in Figs. 12–14. At the start of the downstroke, the introduction of camber reduces the effective angle of attack and, hence, delays the formation of the LEV. This effect is prominent for the low-prestress,
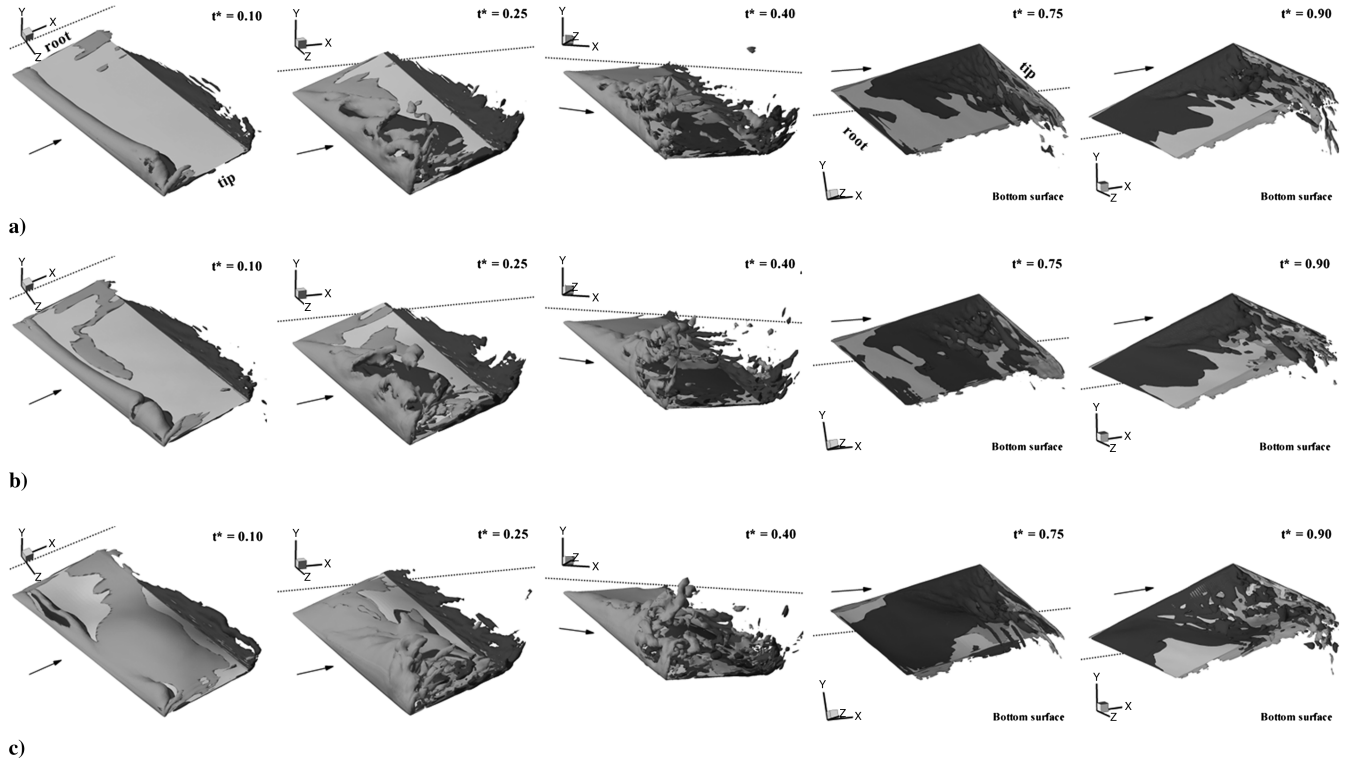
Fig. 11   Isosurface of vorticity ω_ζ at different times for flexible wings with different prestresses: a) 8 N/m b) 4 N/m, and c) 2 N/m. The arrows near the leading edge represent the flow direction, and the dotted lines represent the flapping axis; the root and tip of the wing are marked for better visualization; during upstroke ($t^* = 0.75, 0.90$), the figure shows the bottom surface of the wing.

case C. In Fig. 11, at $t^* = 0.1$ there is no clear formation of the spiral LEV for case C, and the streamlines in Fig. 14 show no formation of the LEV in the chordwise plane at $\zeta = 3$. During the first part of the downstroke, the LEV grows and starts to lift away from the surface for high prestress values. However, for the low-prestress case, due to the introduction of the camber, the LEV does not separate from the wing; instead, it glides over the surface as shown in Fig. 14 at

$t^* = 0.15$. At $t^* = 0.25$, flexible wings introduce positive cambers of the order of 0.05, 0.12, and 0.25 chord for prestresses 8, 4, and 2 N/m, respectively. The location of the maximum camber is near the center of the LEV. In the case of the rigid wing, the LEV separates near the tip as early as $t^* = 0.1$ and lifts off completely from the wing during the middle of the downstroke. In the case of flexible wings, the streamlines in the chordwise plane at $\zeta = 3$ show the presence of
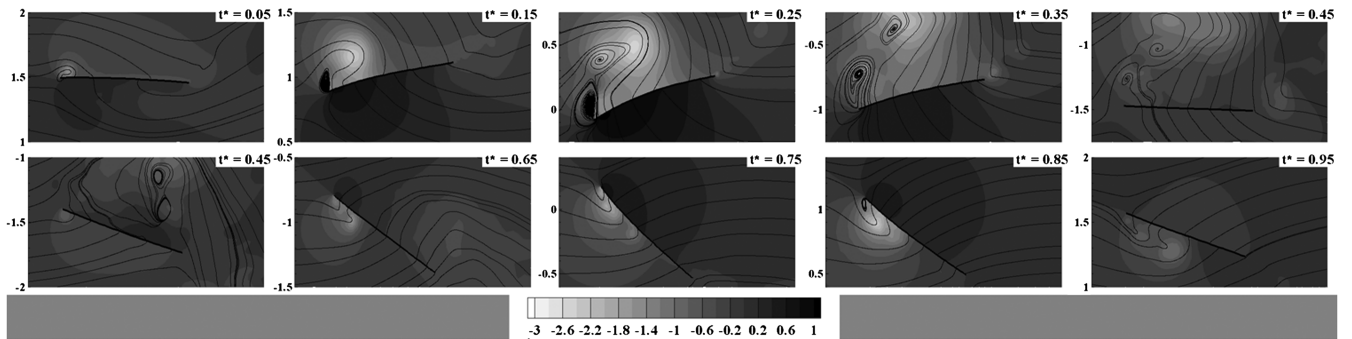
Fig. 12   Instantaneous pressure contours and streamlines in a chordwise plane at $\zeta = 3$ for case A where prestress is 8 N/m.
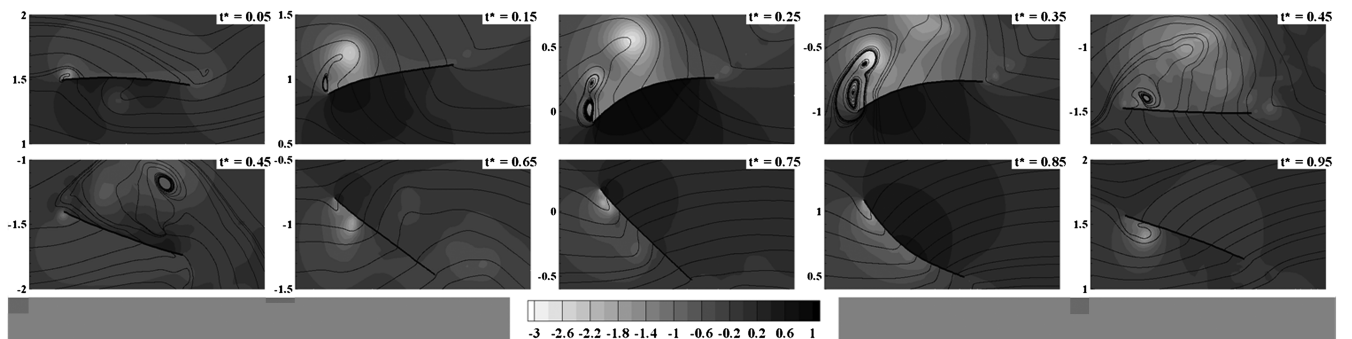
Fig. 13   Instantaneous pressure contours and streamlines in a chordwise plane at $\zeta = 3$ for case B where prestress is 4 N/m.
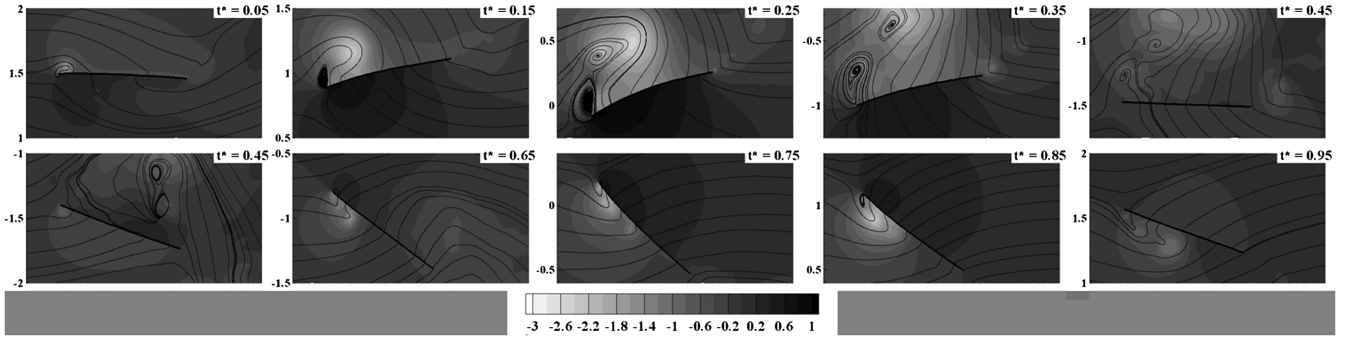
Fig. 14 Instantaneous pressure contours and streamlines in a chordwise plane at $\zeta = 3$ for case C where prestress is 2 N/m.

multiple LEVs for cases A and B, whereas a single attached LEV is observed for case C, covering almost half of the wing from the leading edge. The isosurface vorticity contours shown in Fig. 11 also reflect this phenomenon in which the negative vorticity covers most of the wing surface. This gliding of the LEV due to the camber increases the pressure difference across the wing and results in high force production. In addition, due to the introduction of camber, the resultant force direction shifts toward the forward direction, resulting in a high thrust-to-lift ratio. At $t^* = 0.35$, the LEV starts separating from the wing for all cases and the camber decreases with the location of maximum camber moving toward the trailing edge. During $t^* = 0.4$–0.5, the LEVs dissipate into the flow and only a small portion of the LEV is attached near the base.

During the upstroke, the flexible wings introduce negative camber and the value of camber is high for low prestress. During the first half, a small LEV forms near the tip for all three cases and glides along the camber as shown in Figs. 12–14 during the second half. At the end of the upstroke, the vortex on the bottom surface sheds and dissipates into the flow. The flow structure obtained for case C differs from cases A and B due to the introduction of the uneven camber. At the start of the upstroke, the low prestress has positive deformation near the base due to the unshed LEV formed during the previous downstroke. In addition, the deflection is positive near the trailing edge at $t^* = 0.75$ (Fig. 14) due to shedding of the TEV. This shedding results in a high pressure near the trailing edge for low prestress, which reduces the force production.

2. Lift and Thrust Comparison

The variation of instantaneous lift and thrust coefficients, normalized based on flapping velocity and planform area, is shown

in Fig. 15 for flexible and rigid wings. During the first half of the downstroke, the lift increases due to the formation of the LEV and the maximum value is obtained at around $t^* = 0.25$ for all cases. The maximum value of the lift coefficient increases with camber and a value of around 3 is obtained for low prestress. During the second half of the downstroke, the lift drops due to shedding of the LEV. During the upstroke, the lift is negative and the maximum value of around 1 is obtained at $t^* = 0.825$. The peak negative values of lift for cases A and B are higher than that of the rigid wing, whereas for case C the peak value reduces due to shedding of the TEV and the formation of positive pressure near the trailing edge.

The thrust produced by flapping flight is positive throughout the flapping cycle, and two peaks are produced at around $t^* = 0.25$ and 0.82. The peak value increases with decreasing prestress and a maximum value of 1.6 is obtained for case C. The average values of thrust and lift for all simulations are listed in Table 3. The aeroelastic deformation increases the average values of both lift and thrust. For case C, the values are $C_T = 0.53$ and $C_L = 0.66$, a 43% rise in thrust and an 18% rise in lift when compared to the rigid wing.

E. Effect of Nonuniform Prestress

The analysis of flexible-membrane flapping flight reveals that the introduction of camber increases thrust and lift production significantly. However, the low-prestress case results in deformation even for small differential pressures, resulting in an uneven camber (having both positive and negative displacements at any given instant) during the start of translation and during the upstroke. To reduce this uneven camber, different prestresses are introduced in the spanwise and chordwise directions. Combes and Daniel [25,26] measured the flexural stiffness of wings in both the spanwise and
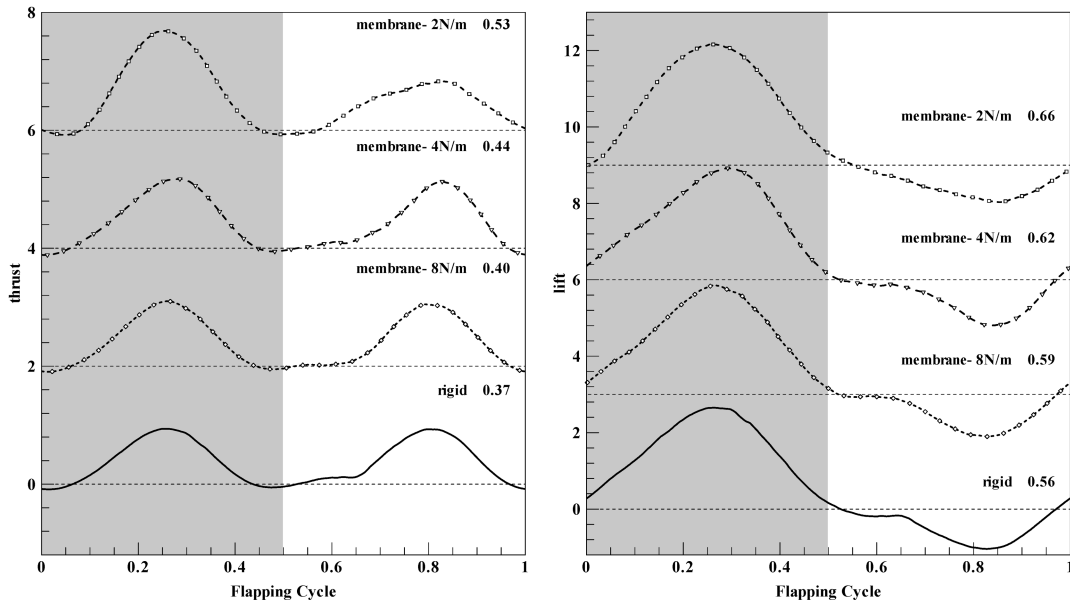

Fig. 15 Comparison of lift and thrust variation of the flexible wings to the rigid wing. The dotted line represents the datum for each profile, and the given values are cycle averaged.

Table 3 Cycle averaged values of lift and drag, power required, and propulsive efficiency

Cases	C_L	C_T	Power flapping	Power rotation	Propulsive efficiency
Rigid	0.56	0.37	1.60	0.20	17.98
A	0.59	0.40	1.65	0.23	18.62
B	0.62	0.44	1.71	0.24	19.74
C	0.66	0.53	1.88	0.21	22.19
D	0.59	0.41	1.66	0.26	18.68
E	0.66	0.50	1.82	0.26	21.03

chordwise directions for 16 insect species. These measurements showed that the spanwise flexural stiffness scaled strongly with the cube of the wingspan, whereas the chordwise flexural stiffness scaled with the square of chord length. Hence, to understand how non-uniform prestresses affect flight performance, two simulations, case D chordwise stiff and case E spanwise stiff (Table 1), are analyzed. The prestress combination of 2 and 8 N/m are used for both simulations. The deformation contours for cases D and E are shown in Fig. 16. In the case of the chordwise stiff wing, the deformation curvature is in the spanwise direction and the maximum deformation is only $0.06C$, which is much lower than that of the low-prestrain case. The maximum deformation is located very near the tip, and the deformation is nonuniform throughout the flapping cycle. In the case of the spanwise stiff wing, the membrane deformation introduces a uniform camber structure, and the deformation is $0.18C$, which is slightly less than that of case C. However, the deformation obtained for case E is not uneven during the start of translation as observed in case C.

The pressure contours and streamlines in the chordwise plane at $\zeta = 3$ for cases D and E are shown in Figs. 17 and 18, respectively. For chordwise stiff wings, the LEV starts to form early and separates from the wing at around $t^* = 0.15$. The streamlines during the middle of the downstroke show the lifting of the LEV and the presence of multiple LEVs. The camber produced is low, and the maximum camber location is at the center of the wing. At the end of the downstroke, the LEV sheds and dissipates into the flow. The camber introduced during the upstroke is very small (-0.04), and the presence of a small vortex is observed during the second half of the upstroke.

In the case of the spanwise stiff wing, the flow structure resembles that of the low-prestrain case. The introduction of camber reduces the effective angle of attack and, hence, delays the formation of the LEV

during the start of the downstroke. At $t^* = 0.25$, a single LEV is observed in the chordwise plane, which then slides over the camber and covers most of the wing surface. At $t^* = 0.25$, the maximum camber location is very close to the leading edge and it moves toward the trailing edge during the second half of the downstroke. The LEV starts to separate from the wing at around $t^* = 0.35$ and sheds into the flow. During the start of the upstroke, the deformation is not large like that of the low-prestrain case. At $t^* = 0.75$, the deformation near the trailing edge is slightly positive and pressure contours do not show positive pressure on the bottom surface as observed in case C. The negative camber is smooth during the second half of the upstroke and a similar vortex gliding effect is observed.

The instantaneous variation of lift and thrust coefficients for cases D and E are compared with the low-prestress case, case C, in Fig. 19. The chordwise stiff wing results in low average values of lift and thrust and the instantaneous values have similar patterns as that of case A. The peak thrust value obtained during the middle of the downstroke is around unity for the chordwise stiff wing, whereas it is 1.6 for the spanwise stiff wing. The average lift value of the spanwise stiff wing matches with that of case C and the average thrust value is 0.5, slightly lower than case C. The results prove that low stiffness along the chordwise direction and high stiffness along the spanwise direction are preferable to obtain better thrust and lift characteristics and a smooth cambering effect.

F. Propulsive Efficiency

The membrane wing shows better aerodynamic performance in terms of lift and thrust than a rigid wing. For a more comprehensive comparison, propulsive efficiencies are computed based on the power required for flapping (P_x) and rotation (P_ζ) for all simulations. The power requirement is computed based on the torque T, generated by the fluid forces and angular velocity of the wing:

$$\mathbf{F} = (p + \tau)\mathbf{d}s \qquad \mathbf{T} = \sum \mathbf{r} \times \mathbf{F} \qquad P = \mathbf{T} \bullet \mathbf{\Omega} \qquad (2)$$

where r is the radius from the axis, p is the pressure, τ is the shear stress, and Ω is the angular velocity of the wing.

The power required for the acceleration of the wing (inertial power requirement) is neglected. The instantaneous variation of the power requirement (normalized based on fluid density, tip velocity, and chord length, $\rho U_f^3 C^2$) for the chordwise stiff wing in case E is shown in Fig. 20. It follows a similar trend as that of lift and thrust. The propulsive efficiency of flapping flight is computed as follows:
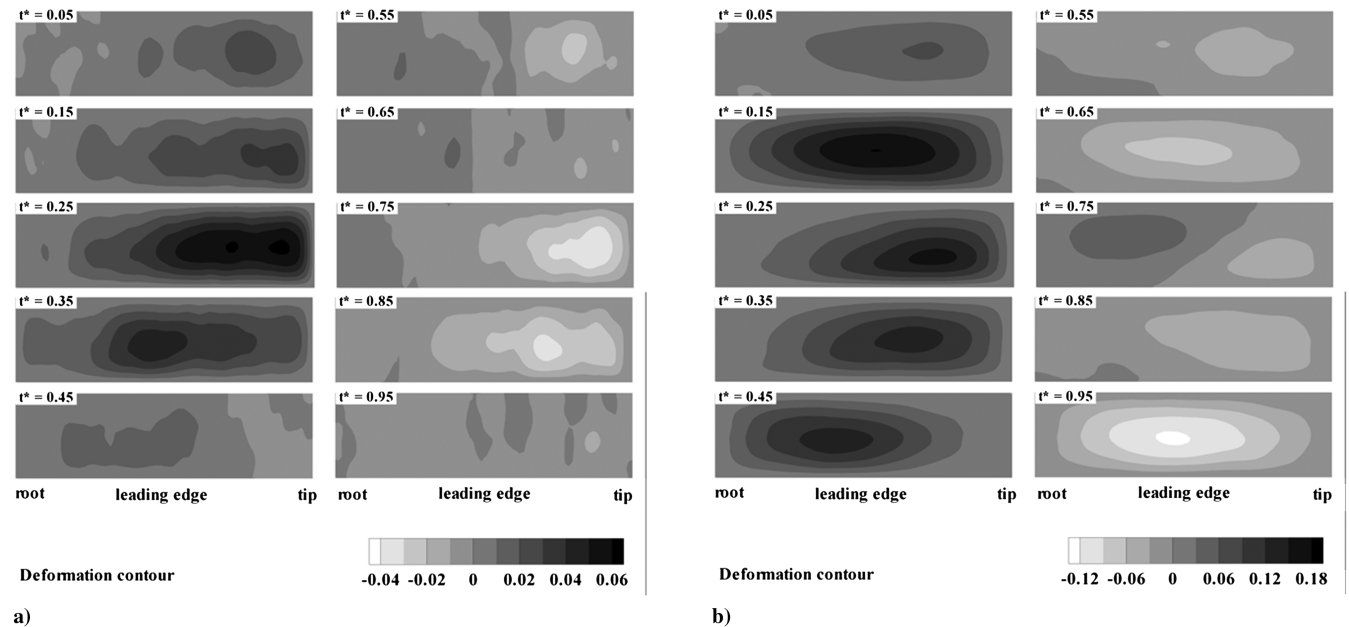
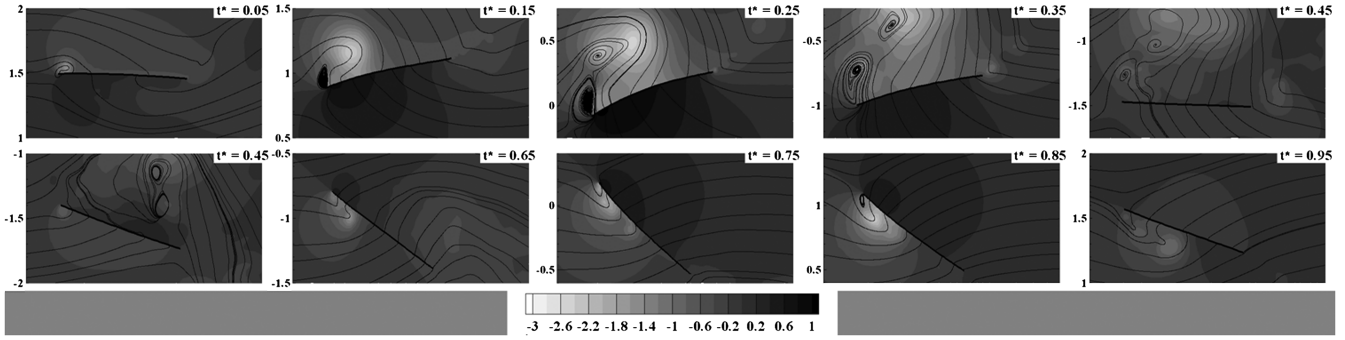**Fig. 16 Deformation contours: a) chordwise stiff wing, and b) spanwise stiff wing.**

Fig. 17 Instantaneous pressure contours and streamlines in a chordwise plane at $\zeta = 3$ for the chordwise stiff wing.
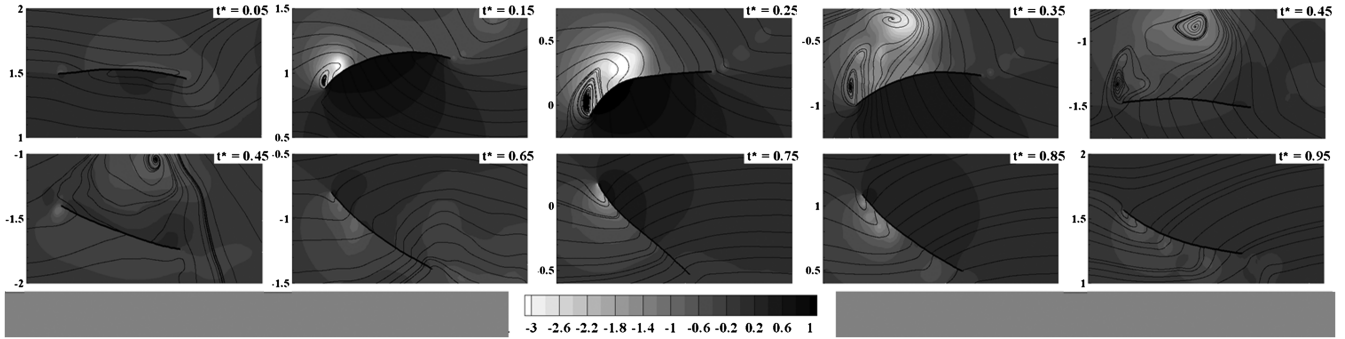

Fig. 18 Instantaneous pressure contours and streamlines in a chordwise plane at $\zeta = 3$ for the spanwise stiff wing.

$$\eta_{\text{prop}} = \frac{F_T u_\infty}{P_x + P_\zeta} \qquad (3)$$

The average values of power requirement and propulsive efficiency for all simulations are given in Table 3. The performance of all flexible wing configurations is better than that of a rigid wing. The low-prestress case offers the best propulsive efficiency of 22%, followed by the spanwise stiff wing at 21%.

G. Inertial Forces and Nonlinearity

In the current study, only the aerodynamic force is considered to compute the out-of-plane displacement of the membrane wing. However, for high-frequency flapping flight, inertial forces could be as high as pressure forces. An estimation of the inertial force for case B is made based on the kinematics:

$$F_{\text{iner}} = -\rho_w h_w (\dot{V} + \dot{\Omega} \times r + 2\Omega \times V + \Omega \times \Omega \times r) \qquad (4)$$

Figure 21 shows a comparison of the inertial forces in the out-of-plane direction with pressure forces for case B. The direction of inertial forces changes during translation. During the first half of the downstroke, the inertial force is positive (acting upward) and it is negative during the second half of the downstroke. In addition, the inertial force due to rotation produces a diagonal pattern across the membrane surface. The comparison shows that the maximum values of the inertial forces are almost of the same order as the peak pressure force. However, in practice, the mass of the wing will not be uniform; hence, for estimating the true effect of inertial forces, a separate study with the actual wing mass distribution is required.

For aeroelastic analysis, the current study employs a linear membrane model. This model is strictly valid only if the in-plane stresses developed by the out-of-plane deformation are much smaller
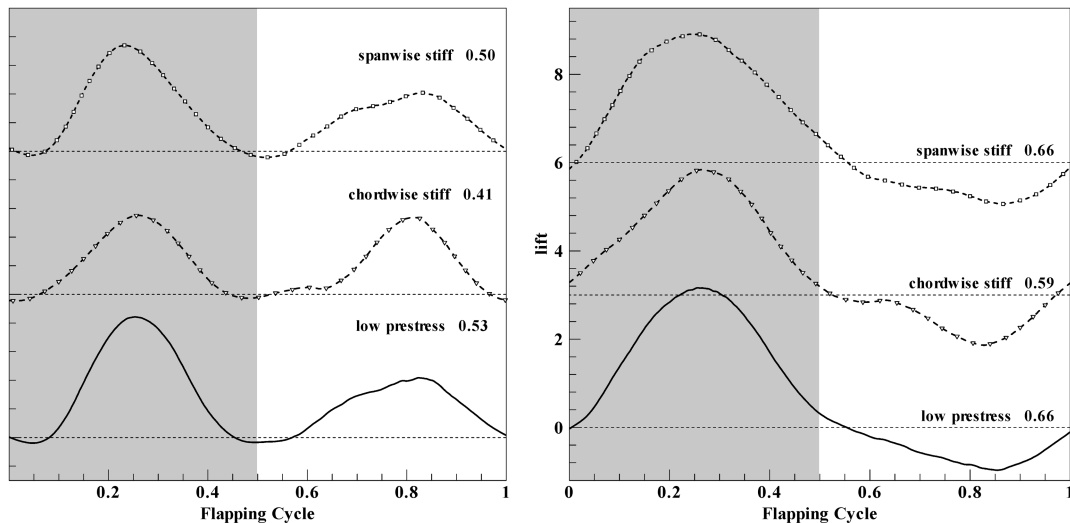

Fig. 19 Variation of lift and thrust for prestress cases C–E. The dotted line represents the datum for each profile, and the given values are cycle averaged.
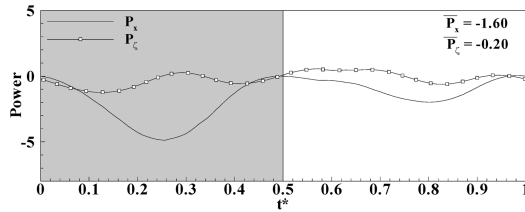
Fig. 20   Instantaneous variation of power requirement for the spanwise rigid wing (case E).

than the initial prestress values. To evaluate this assumption, the in-plane stresses are computed for case B based on the following deformation:

$$\sigma_\xi = E \frac{1}{2} \left(\frac{\partial w}{\partial \xi} \right)^2 \qquad \sigma_\zeta = E \frac{1}{2} \left(\frac{\partial w}{\partial \zeta} \right)^2 \qquad (5)$$

where E is Young's modulus, which is taken as 2 GPa for polyester. Figure 22 shows the contours of $\sigma^* h_w$ along the chordwise and spanwise directions for case B during the middle of the downstroke at $t^* = 0.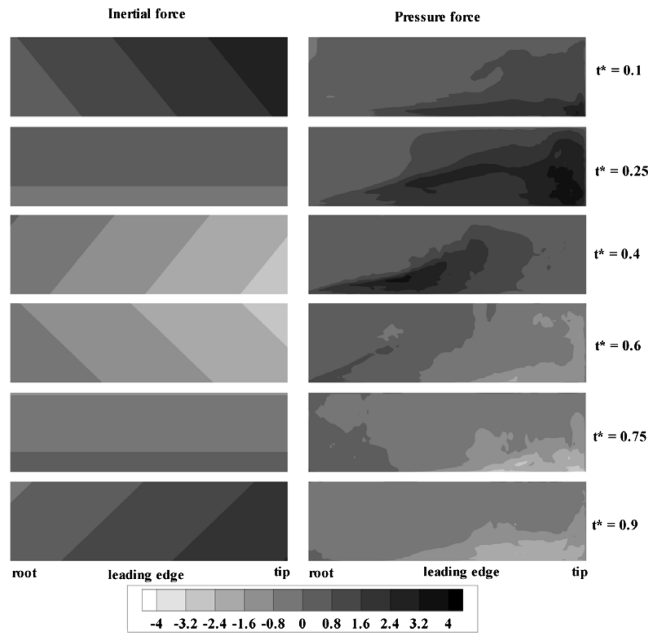25$. The stress values near the tip and near the leading and trailing edges are higher due to the zero displacement boundary conditions. However, the stress on most of the wing surface is low, of the order of 0.01 N/m, which signifies that the linear assumption is valid on most of the wing surface.
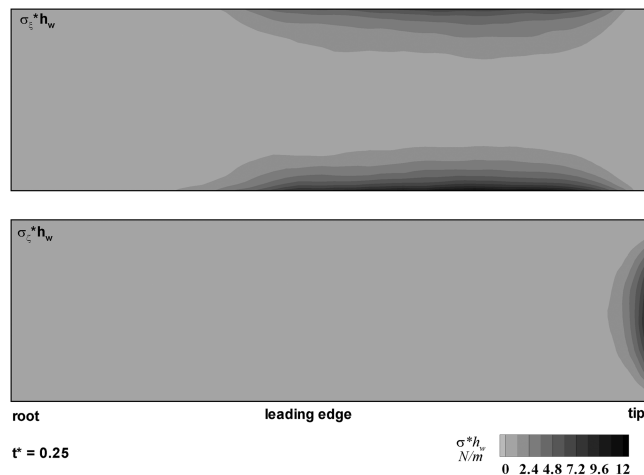
IV.   Conclusions

The effect of aeroelastic cambering on flapping flight performance is analyzed using a linear elastic membrane model. All the simulations are carried out at $Re = 10,000$ for a forward flight with an advance ratio of 0.5 with similar kinematics. The simulation is carried out for a rigid wing and for flexible wings with different prestress values. The flow structure for the rigid wing shows the formation of a spiral LEV during the downstroke, which results in high thrust and lift values. However, the LEV lifts off from the surface during the middle of the downstroke and sheds, leading to a drop in lift and thrust. In the case of flexible wings, a positive and a negative camber are introduced during the downstroke and upstroke, respectively. The introduction of camber increases lift and thrust production and results in high propulsive efficiency. The main reason for increased performance is the gliding of the LEV along the camber, which delays the lifting off of the LEV from the surface. Because of gliding, the LEV covers most of the wing surface, resulting in high force production. In addition, introduction of the camber also increases the contribution of the resultant force to the thrust. In comparison with a rigid wing, a 40% increase in thrust and a 20% increase in lift are observed for a low-prestress membrane. However, the deformation for this low-prestress case is highly uneven, with both negative and positive deformations at the same instant in time. To avoid this uneven camber formation, simulations are carried out with directionally biased prestress values. The results from these simulations show that the membrane with a low prestress along the chord and a high prestress along the span offers the best aerodynamics and aeroelastic performance.

In conclusion, the current study validates previous observations made for fixed wings that aeroelastic cambering is beneficial to the aerodynamic performance of flapping flight. This result can also be extended to design morphing wings that change camber to adjust to unsteady aerodynamics for maximum performance.

Fig. 21   Comparison of inertial and pressure forces at different instances for case B.

Acknowledgments

References

[1] McMasters, J. H., and Henderson, M. L., "Low Speed Single Element Airfoil Synthesis," CP 2085, Part 1, NASA, Hampton, VA, 1979, pp. 1–32.

[2] Weis-Fogh, T., "Quick Estimate of Flight Fitness in Hovering Animals, Including Novel Mechanisms for Lift Production," *The Journal of Experimental Biology*, Vol. 59, 1973, pp. 169–230.

[3] Dickinson, M. H., and Götz, K. G., "Unsteady Aerodynamic Performance of Model Wings at Low Reynolds Numbers," *The Journal of Experimental Biology*, Vol. 174, 1993, pp. 45–64.

[4] Ellington, C. P., Berg, C. V. D., Willmott, A. P., and Thomas, A. L. R., "Leading-Edge Vortices in Insect Flight," *Nature (London)*, Vol. 384, 1996, pp. 626–630.
      doi:10.1038/384626a0

[5] Dickinson, M. H., Lehmann, F.-O., and Sane, S. P., "Wing Rotation and the Aerodynamic Basis of Insect Flight," *Science*, Vol. 284, 1999, pp. 1954–1960.
      doi:10.1126/science.284.5422.1954

[6] Ellington, C. P., "The Novel Aerodynamics of Insect Flight: Applications to Micro-Air Vehicles," *The Journal of Experimental Biology*, Vol. 202, 1999, pp. 3439–3448.

[7] Liu, H., Ellington, C. P., Kawachi, K., Berg, C. V. D., and Willmott1, A. P., "A Computational Fluid Dynamic Study of Hawkmoth

Fig. 22   Contours of in-plane stress due to out-of-plane displacement for case B at $t^* = 0.25$.

Hovering," *The Journal of Experimental Biology*, Vol. 201, 1998, pp. 461–477.

[8] Birch, J. M., and Dickinson, M. H., "Spanwise Flow and the Attachment of the Leading-Edge Vortex on Insect Wings," *Nature*, Vol. 412, Aug. 2001, pp. 729–733.
doi:10.1038/35089071

[9] Gopalakrishnan, P., and Tafti, D. K., "Effect of Rotation and Angle of Attack on Force Production of Flapping Flights," *AIAA Journal*, Vol. 47, No. 11, Nov. 2009, pp. 2505–2518.
doi:10.2514/1.37540

[10] Gopalakrishnan, P., and Tafti, D. K., "Effect of Phasing of Rotation on Delayed Stall in Flapping Flights Related to MAVs at $Re = 10^4$," AIAA Paper 2008-4301, June 2008.

[11] Wang, H., Zeng, L., Liu, H., and Yin, C., "Measuring Wing Kinematics, Flight Trajectory and Body Attitude During Forward Flight and Turning Maneuvers in Dragonflies," *The Journal of Experimental Biology*, Vol. 206, 2003, pp. 745–757.
doi:10.1242/jeb.00183

[12] Tobalske, B. W., Warrick, D. R., Clark, C. J., Powers, D. R., Hedrick, T. L., Hyder, G. A., and Biewener, A. A., "Three-Dimensional Kinematics of Hummingbird Flight," *The Journal of Experimental Biology*, Vol. 210, 2007, pp. 2368–2382.
doi:10.1242/jeb.005686

[13] Liu, T., Kuykendoll, K., Rhew, R., and Jones, S., "Avian Wing Geometry and Kinematics," *AIAA Journal*, Vol. 44, No. 5, May 2006, pp. 954–963.
doi:10.2514/1.16224

[14] Shyy, W., Berg, M., and Ljungqvist, D., "Flapping and Flexible Wings for Biological and Micro Air Vehicles," *Progress in Aerospace Sciences*, Vol. 35, 1999, pp. 455–505.
doi:10.1016/S0376-0421(98)00016-5

[15] Ho, S., Nassef, H., Pornsinsirirak, N., Tai, Y.-C., and Ho, C.-M., "Unsteady Aerodynamics and Flow Control for Flapping Wing Flyers," *Progress in Aerospace Sciences*, Vol. 39, 2003, pp. 635–681.
doi:10.1016/j.paerosci.2003.04.001

[16] Shyy, W., Jenkins, D. A., and Smith, R. W., "Study of Adaptive Shape Airfoils at Low Reynolds Number in Oscillatory Flows," *AIAA Journal*, Vol. 35, No. 9, April 1997, pp. 1545–1548.
doi:10.2514/2.7484

[17] Shyy, W., Klevebring, F., Nilsson, M., Sloan, J., Carroll, B., and Fuentes, C., "Rigid and Flexible Low Reynolds Number Airfoils," *Journal of Aircraft*, Vol. 36, No. 3, May 1999, pp. 523–529.
doi:10.2514/2.2487

[18] Smith, M. J. C., "Simulating Moth Wing Aerodynamics: Towards the Development of Flapping-Wing Technology," *AIAA Journal*, Vol. 34, No. 7, 1996, pp. 1348–1355.
doi:10.2514/3.13239

[19] Stanford, B., and Ifju, P., "Membrane Micro Air Vehicles with Adaptive Aerodynamic Twist: Numerical Modeling," AIAA Paper 2007-1758, April 2007.

[20] Stanford, B., Albertani, R., Viieru, D., Shyy, W., and Ifju, P., "Static Aeroelastic Model Validation of Membrane Micro Air Vehicle Wings," AIAA Paper 2007-1067, Jan. 2007.

[21] Stanford, B., Sytsma, M., Albertani, R., Viieru, D., Shyy, W., and Ifju, P., "Static Aeroelastic Model Validation of Membrane Micro Air Vehicle Wings," *AIAA Journal*, Vol. 45, No. 12, Dec. 2007, pp. 2828–2837.
doi:10.2514/1.30003

[22] Gopalakrishnan, P., and Tafti, D. K., "A Parallel Boundary Fitted Dynamic Mesh Solver for Applications to Flapping Flight," *Computers and Fluids*, Vol. 38, 2009, pp. 1592–1607.
doi:10.1016/j.compfluid.2009.01.006

[23] Gopalakrishnan, P., and Tafti, D. K., "A Parallel Multiblock Boundary Fitted Dynamic Mesh Solver for Simulating Flows with Complex Boundary Movement," AIAA Paper 2008-4142, June 2008.

[24] Banerjee, S. P., and Patil, M. J., "Aeroelastic Analysis of Membrane Wings," AIAA Paper 2008-1812, April 2008.

[25] Combes, S. A., and Daniel, T. L., "Flexural Stiffness in Insect Wings I. Scaling and the Influence of Wing Venation," *The Journal of Experimental Biology*, Vol. 206, No. 17, Sept. 2003, pp. 2979–2987.
doi:10.1242/jeb.00523

[26] Combes, S. A., and Daniel, T. L., "Flexural Stiffness in Insect Wings II. Spatial Distribution and Dynamic Wing Bending," *The Journal of Experimental Biology*, Vol. 206, No. 17, Sept. 2003, pp. 2989–2997.
doi:10.1242/jeb.00524

P. Beran
Associate Editor